ACS NANO

www.acsnano.org

ARTICLE

Low-Temperature Contacts and the Coulomb Blockade Effect in Layered Nanoribbons with In-Plane Anisotropy

Ivan A. Verzhbitskiy,* Abhishek Mishra, Sanchali Mitra, Zhepeng Zhang, Sarthak Das, Chit Siong Lau, Rainer Lee, Ding Huang, Goki Eda, Yee Sin Ang, and Kuan Eng Johnson Goh*

Cite This: *ACS Nano* 2025, 19, 10878–10888

Read Online

ACCESS | Metrics & More | Article Recommendations | Supporting Information

ABSTRACT: One-dimensional (1D) nanoribbons (NRs) constitute rapidly advancing nanotechnology with significant potential for emerging applications such as quantum sensing and metrology. TiS_3 nanoribbons exhibit strong in-plane crystal anisotropy, enabling robust 1D confinement and resilience to edge disorder. Nevertheless, charge transport in 1D TiS_3 remains relatively unexplored, particularly at low temperatures, where high contact resistance impacts device performance and fundamentally limits its applications. Here, we engineer electrical contacts between a bulk metal and a 1D NR and explore the low-temperature characteristics of the 1D field-effect devices. We report ohmic contacts for 1D TiS_3 with temperature-independent contact resistances as low as 2.7 ± 0.3 kΩ·μm, enabling the study of charge transport at low temperatures (down to 35 mK) and clear observation of the Coulomb blockade effect. We demonstrate single-electron transport in 1D TiS_3 and perform excited state spectroscopy and magnetospectroscopy, extracting an out-of-plane electron *g*-factor, $g = 1.8 \pm 0.3$.

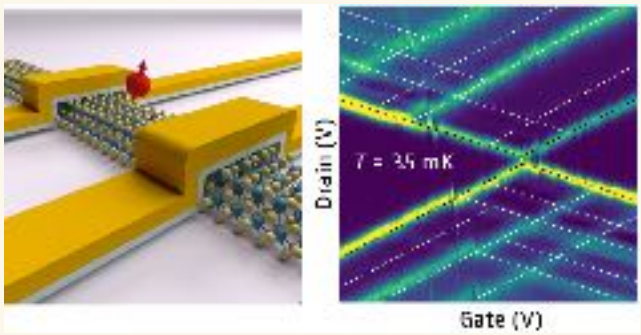

KEYWORDS: *van der Waals, titanium trisulfide, 1D, ohmic contacts, quantum dot, single-electron transistor*

1. INTRODUCTION

The relentless drive for advancements in energy-efficient electronics and quantum technologies has positioned layered van der Waals (vdW) materials at the forefront of fundamental research and technological innovation.[1] Among the various layered materials, one-dimensional (1D) nanoribbons (NRs) have emerged as a particularly compelling vdW system.[2−4] While graphene or MoS_2 NRs are celebrated for their high carrier mobility[5] or spin/valley-polarized edges,[6,7] their electronic band structures are highly sensitive to width and edge termination.[8,9] This inherent structural dependence, however, exposes 1D NR devices to edge disorder, owing to challenges in maintaining structural homogeneity during the chemical synthesis.[10,11] Such disorder constrains charge transport efficiency in 1D field-effect transistors (FETs), compromises their reproducibility and scalability, and introduces noise from uncontrollable edge states in quantum devices.[12,13]

Titanium trisulfide (TiS_3) is a layered vdW semiconductor with a quasi-1D morphology.[14] Unlike isotropic vdW materials such as graphene or MoS_2, TiS_3 exhibits strong in-plane crystal anisotropy[15] that translates into anisotropic thermal and charge transport,[14] motivating exploration toward thermoelectric[16,17] and optoelectronic[18,19] applications. A single layer of TiS_3 consists of 1D-like covalently bonded atomic chains held together by considerably weaker interatomic coupling (Figure 1a), ensuring NR morphology with consistent width and edge termination.[20] The electronic band gap of ∼1 eV varies little with thickness or stacking order and, importantly, shows weak dependence on the width of the NRs, particularly in the limit of few-atom-wide chains,[21,22] further reducing the impact of edge disorder. Therefore, semiconducting TiS_3 NRs, with their inherent 1D confinement and resilience to edge disorder, demonstrate significant potential for nanoelectronics and quantum devices, like single-electron charge sensors[23] and pumps.[24]

Received: October 24, 2024
Revised: February 13, 2025
Accepted: February 14, 2025
Published: March 13, 2025

https://doi.org/10.1021/acsnano.4c15086
ACS Nano 2025, 19, 10878−10888

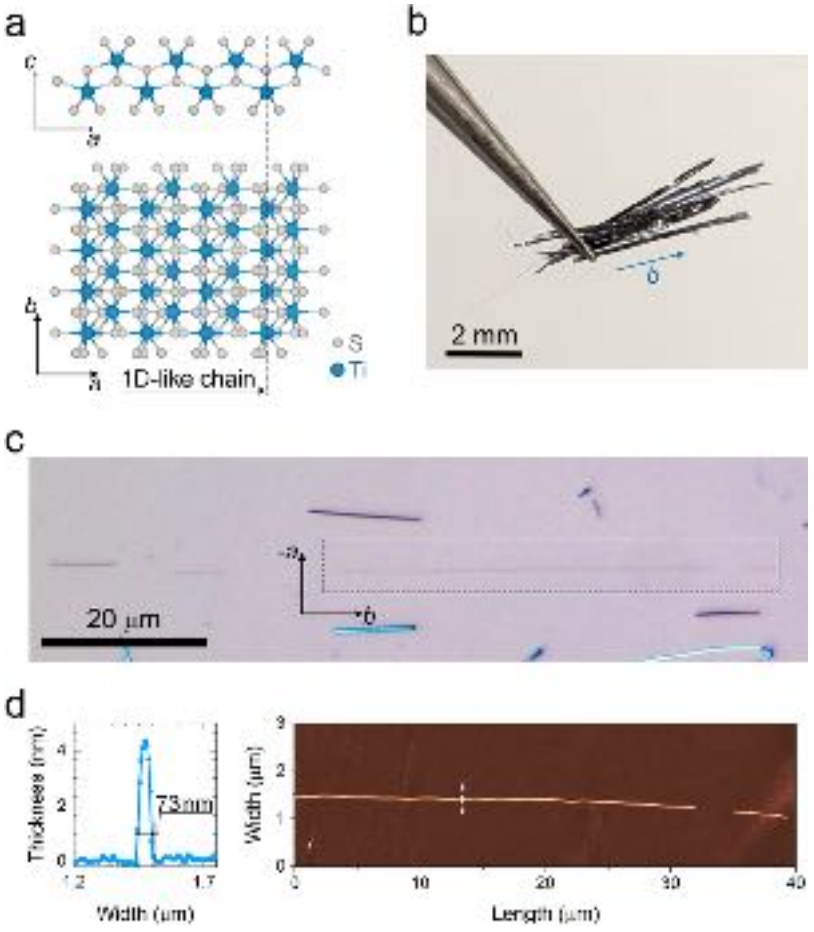

Figure 1. (a) Ball-and-stick model of the TiS_3 crystal structure in the *ac* plane (top) and *ab* plane (bottom); (b) optical image of as-grown TiS_3 crystals; (c) optical image of TiS_3 NRs exfoliated on a SiO_2/Si wafer; (d) atomic force microscopy (AFM) profile (left) and topography (right) of the TiS_3 NR outlined by the dashed line in (c).

The semiconducting n-type behavior of TiS_3 NR FETs has been established through several recent reports.[15,25−27] Below 200 K, thin 1D TiS_3 devices exhibit decreased performance, entering a high-resistivity state below 100 K.[27] While the nature of this behavior remains an open question,[28,29] these studies report nonlinear output characteristics of Cr/Au and Ti/Au contacts at low temperatures, hindering the device potential for 1D cryoelectronics and quantum applications. In general, poor contacts degrade charge transport, particularly at low temperatures, leading to energy dissipation and noise, which limits sensitivity and control over electron flow in nanoscale devices.[30,31] In quantum devices like single-electron transistors, high contact resistance impedes electron tunneling by introducing additional barriers and traps, increases thermal broadening of energy levels, and blurs the distinction between charge states, reducing the ability to resolve single-electron events.[32−34]

While high contact resistance in 1D devices is a long-standing challenge,[35] experimental studies on metal-1D contacts for emergent technologies like 1D vdW NRs are particularly scarce.[2] Contact engineering methods developed for bulk semiconductors[36] have proved challenging for vdW materials.[37,38] Typically, the deposition of a bulk, three-dimensional metal on the surface of a vdW semiconductor results in the formation of a Schottky barrier, even if the metal work function aligns with the semiconductor's electron affinity.[38] This occurs because high kinetic energy transfer and chemical bonding at the interface damage the fragile vdW semiconductor surface,[39] leading to Fermi-level pinning near the band edge and high contact resistance.[40] Efforts to reduce contact resistance in 1D vdW NR devices are further encumbered by the limited area available for contact.[41] Thus, realizing clean, microscopic contacts to 1D vdW NRs with low contact resistance and near-zero Schottky barrier heights presents an exceptional challenge.

In this article, we present a comprehensive in-depth analysis of electrical contacts and low-temperature charge transport in 1D vdW semiconductor TiS_3. We demonstrate the realization of ultraclean contacts for 1D TiS_3 FETs that exhibit ohmic characteristics down to 5 K. This achievement builds on recent findings that the gentle deposition of low-melting-point metals, such as indium (In), preserves the vdW surface of monolayer MoS_2.[42] In our In-TiS_3 devices, the contact resistance remains below 3 kΩ·μm across the entire temperature range studied, representing one of the lowest contact resistances reported for 1D semiconducting vdW NRs. We provide insights into the origin of this low contact resistance using density functional theory (DFT) calculations, which reveal a dipole-like charge redistribution at the In-TiS_3 interface and interfacial charge transfer that ensures ohmic behavior, particularly at low temperatures. In contrast, we demonstrate through both theory and experiment that conventional contact materials, such as gold (Au), exhibit more than an order of magnitude higher contact resistance, resulting in nonohmic contacts and

https://doi.org/10.1021/acsnano.4c15086
ACS Nano 2025, 19, 10878−10888

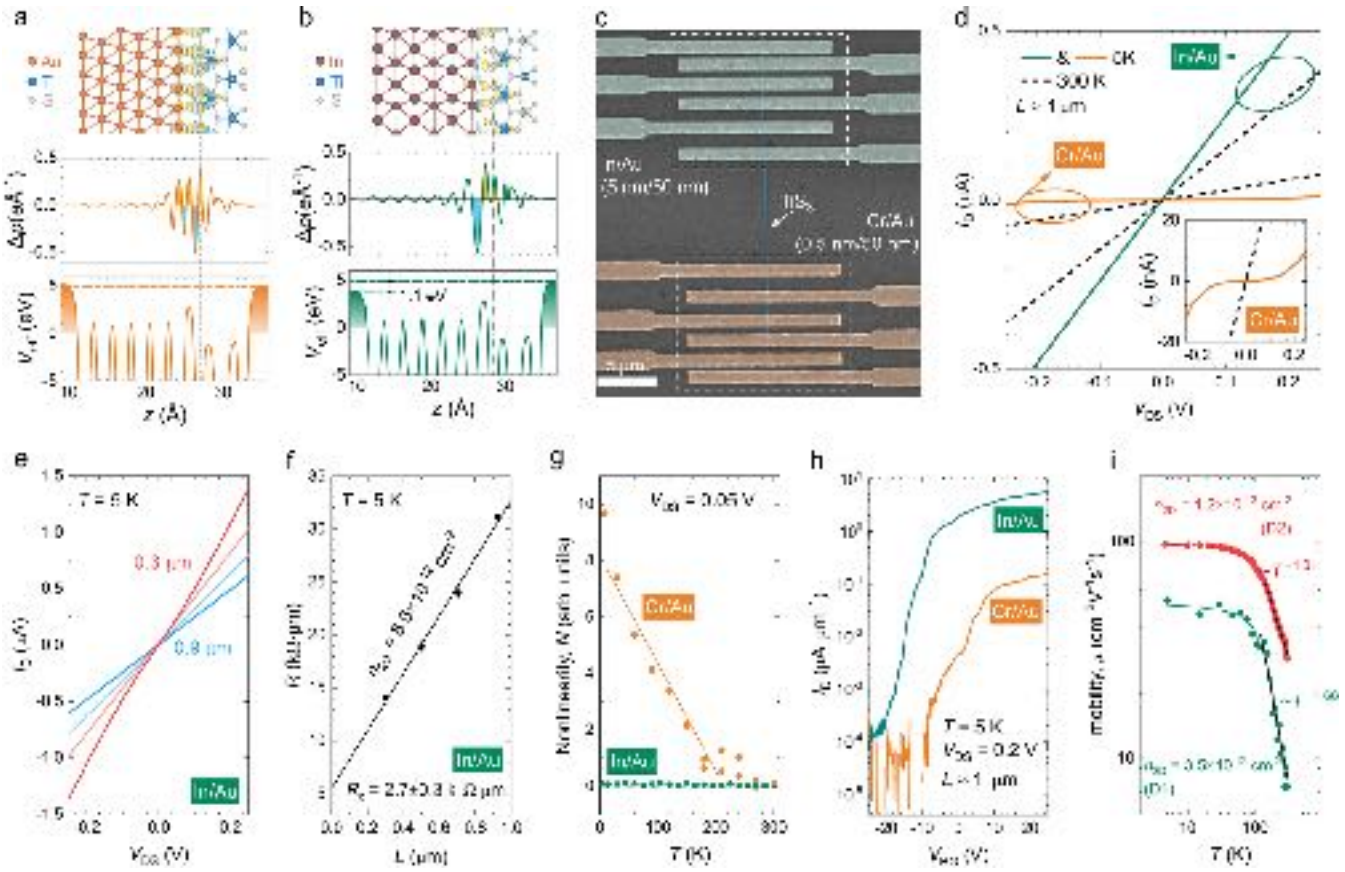

Figure 2. (a, b) Interface models for Au−TiS_3 and In−TiS_3 metal−semiconductor junctions, respectively. The top panels show DFT-optimized atomic geometries with interfacial charge distribution overlays at the junction. The isosurface level is 1 × 10^{-3} $eÅ^{-1}$. The middle panels show the plane-averaged charge density difference ($\Delta\rho$), while the bottom panels plot the minimum effective potential (V_{eff}) across the interface. (c) False-color scanning electron microscopy (SEM) image of two sets of devices (outlined with white dashed lines) fabricated with In/Au and Cr/Au electrodes. Scale bar: 5 μm. (d) Output curves at 5 and 300 K for devices with Cr/Au and In/Au electrodes, with a channel length of ∼1 μm at a carrier density of 8.6 × 10^{12} cm^{-2}. The rescaled plot of the Cr/Au device highlights the nonlinear characteristics at 5 K in the inset. (e) Linear output characteristics at a carrier density of 8.6 × 10^{12} cm^{-2} and 5 K for the device with In/Au electrodes, with channel lengths ranging from 0.3 to 0.9 μm. (f) Contact resistance extraction for In/Au electrodes using the transfer length method (TLM) at 5 K. (g) Nonlinearity (N) as a function of temperature for Cr/Au and In/Au devices, defined as $N = (d^2I_{DS}/dV_{DS}^2)/2(dI_{DS}/dV_{DS})$ at a carrier density of 8.6 × 10^{12} cm^{-2}. (h) Transfer characteristics of 1D TiS_3 FETs with Cr/Au and In/Au contacts, both having a channel length of ∼1 μm, at 5 K and V_{DS} = 0.2 V. (i) Logarithmic plot of the field-effect mobility evolution with temperature for carrier densities of 3.5 × 10^{12} cm^{-2} (green symbols, device D1) and 1.2 × 10^{13} cm^{-2} (red symbols, device D2). Solid green and red lines are a guide to the eye. The solid black lines represent fits to the power law $\mu \sim T^{-\gamma}$. Both devices D1 and D2 were made with In/Au contacts.

significantly degrading FET performance. Efficient charge injection from high-quality contacts allows us to access the quantum tunneling regime in 1D TiS_3 NRs, where we observe the Coulomb blockade effect in two-probe short-channel (200 nm) devices at 35 mK. We conduct excited state spectroscopy and report on spin filling and magnetospectroscopy of the ground states, demonstrating a single-electron transistor in TiS_3 NRs. These results highlight TiS_3 as a promising material platform for 1D cryoelectronics and emerging quantum technologies, including quantum sensing and quantum information processing.

2. RESULTS AND DISCUSSION

TiS_3 forms a layered structure in which atomically thin sheets are held together by weak vdW forces. The strong crystal anisotropy is evident from the distinct atomic arrangement in the basal plane (Figure 1a), which promotes unidirectional crystal growth along the crystallographic b-axis (Figure 1b). Due to considerably weaker interatomic interactions along the a-axis,[20] micromechanical exfoliation yields long and narrow NRs. Figure 1c shows an exfoliated NR (outlined in the rectangle), measuring over 30 μm in length, 73 nm in width, and 4.3 nm in thickness (Figure 1d). Raman spectroscopy and X-ray diffraction analysis confirm the monoclinic structure of as-grown TiS_3 crystals (Supporting Figures S1 and S2), consistent with the previous reports.[43,44]

2.1. Engineering Low-Temperature Contacts. For a comprehensive comparative analysis of metal contacts on 1D TiS_3, we systematically evaluated the contact characteristics of the In−TiS_3 and Au−TiS_3 interfaces. To understand the atomistic interactions at the metal−semiconductor junctions, we modeled the electronic structures and charge redistribution properties at both interfaces using DFT calculations. Figure 2a,b shows the simulated atomic structures at the Au−TiS_3 and In−TiS_3 interfaces, respectively. The optimized interface geometry (Figure 2a,2b and Supporting Figure S3) indicates that the gap between In and TiS_3 surface layers (∼3.1 Å) closely matches the interlayer distance in the bulk of vdW crystal (∼3.2 Å), suggesting minimal perturbation at the In−TiS_3 interface. This preserved interlayer distance implies the

https://doi.org/10.1021/acsnano.4c15086
ACS Nano 2025, 19, 10878−10888

clean, strain-free nature of indium contacts, as previously observed with layered two-dimensional (2D) materials like MoS_2.[42] In contrast, the reduced gap at the Au−TiS_3 interface (~2.7 Å) points to contact-induced structural distortions that may lead to the disordered interface, likely accompanied by chemical-like bonding.[45] Ideally, interfacial interactions at a metal−semiconductor junction enhance the carrier injection efficiency. However, strong interaction between the vdW semiconductor surface and the contact metal can adversely affect the device performance.[38] Such interactions at the interface may induce midgap states, effectively pinning the Fermi level below the conduction band.[46] This pinning can result in the formation of a Schottky barrier, leading to an increased contact resistance. This issue, however, can be mitigated by inserting a buffer layer of graphene[47] or hexagonal boron nitride (hBN)[48] between the metal and the semiconductor, thus weakening their interaction.[49]

The fundamental difference between In−TiS_3 and Au−TiS_3 is further corroborated by interfacial charge redistribution, shown in Figure 2a,2b as it overlays the optimized atomic geometries (top panels), as well as plane-averaged charge density difference along the z-direction orthogonal to the interface ($\Delta\rho$, middle panels). The latter is defined as the difference of total charge density of the full system (ρ_{tot}) and the constituent subsystems, such as the 3D metal (ρ_M) and the freestanding TiS_3 (ρ_{TiS_3}),

$$\Delta\rho = \rho_{tot} - \rho_M - \rho_{TiS_3} \quad (1)$$

The complex nature of charge redistribution at the Au−TiS_3 interface is evident from the multiple peaks and valleys in $\Delta\rho$ within the interface gap, as shown in Figure 2a, middle panel. Note that a positive $\Delta\rho$ peak indicates electron accumulation, while a negative valley represents electron depletion. Notably, we found that at the Au−TiS_3 interface, charge accumulates in the middle of the gap, depleting both Au and TiS_3 surface layers. This behavior resembles covalent-like quasi-bonding, previously observed in metal−vdW junctions such as Mo_2CF_2−MoS_2, and is similar to interlayer hybridization seen in several 2D vdW materials.[50] As a result, there is net zero charge transfer across the Au−TiS_3 interface. The presence of charge states in the interface gap can easily pin the Fermi level inside the band gap of TiS_3, forming a Schottky barrier. In contrast, the electron redistribution at the In−TiS_3 interface (Figure 2b, middle panel) exhibits a simpler, dipole-like behavior. The band alignment of the TiS_3 band edge and the In Fermi level induces electron charge transfer toward the TiS_3 site. The electron flow across the In−TiS_3 interface is further supported by the effective potential (V_{eff}) plot shown in the bottom panel of Figure 2b. Unlike the Au−TiS_3 case (Figure 2a, bottom panel), the positive potential difference of ~1.1 eV gained over the In−TiS_3 junction ensures efficient electron transfer from the metal contact to the 1D semiconductor. This implies a vanishing Schottky barrier at the interface and strong n-doping of the TiS_3 at the contact region,[50] which is further confirmed by our DFT band structure calculations (Supporting Figure S4). Considering the soft nature of low-melting-point metals like indium,[42] these theoretical observations suggest that evaporated 3D In forms a clean vdW contact with 1D TiS_3, ensuring efficient electron injection across the junction.

Armed with these insights, we experimentally examined 1D TiS_3 devices by carefully measuring contact resistance using the transfer length method (TLM) and accessing typical FET characteristics at temperatures down to 5 K. To this end, a thin (d = 7.3 nm) and narrow (W = 76 nm) NR was selected from the TiS_3 crystals that were mechanically exfoliated on a SiO_2/Si substrate (90 nm oxide thickness). We designed and fabricated two sets of TLM structures on the same NR to compare typical Cr/Au contacts with the vdW contacts made by 5 nm of In and capped with 50 nm of Au (In/Au). During the metal deposition for Cr/Au contacts, we adjusted the Cr layer thickness to 0.5 nm to minimize potential damage to TiS_3 from high-energy Cr atoms while ensuring strong adhesion of the contacts to the substrate. Anticipating that the Cr layer, despite its thinness, may still induce changes to the Au−TiS_3 interface,[51] we theoretically examined the Cr-TiS_3 interface (Supporting Discussion V and Supporting Figure S5). Similar to Au, Cr significantly disrupts the TiS_3 surface at the interface, leading to chemical bond-like interactions that may negatively affect the carrier injection efficiency.

Figure 2c shows a false-color SEM image of the two structures fabricated side-by-side on the same TiS_3 NR. Output curves for ~1 μm channel devices with Cr/Au and In/Au contacts are shown in Figure 2d. Both devices exhibit linear characteristics at room temperature, although the current in Cr/Au devices is considerably lower. Notably, only In/Au contacts display linear characteristics at 5 K. The nonlinear output curves for Cr/Au contacts at low temperatures (inset in Figure 2d) suggest the presence of energy barriers at the metal−TiS_3 junction, similar to those reported for 2D vdW semiconductors.[38] This observation aligns with the decrease in current in Cr/Au devices, where energy barriers cause significant contact resistance, increasing the total resistance of the device by nearly an order of magnitude (Supporting Figure S6). To eliminate the potential influence of the Cr layer on carrier injection efficiency, we fabricated devices using pure Au electrodes (Supporting Discussion VIII and Supporting Figure S7). Similar to Cr/Au−TiS_3 devices, pure Au contacts exhibit nonlinear output characteristics below 300 K, indicating nonohmic carrier injection at low temperatures.

Following the TLM analysis of the In/Au devices (Figure 2e,f and Supporting Figure S8), we extracted a contact resistance of 2.7 ± 0.3 kΩ·μm at a base temperature of 5 K and a carrier density of 8.6 × 10^{12} cm^{-2}. To the best of our knowledge, this is among the lowest values reported for 1D MoS_2 and TiS_3 NRs, outperforming the contact resistance of conventional 3D metal contacts to 1D NRs, such as Sc/Ni (39.6 kΩ·μm at 300 K),[52] Ni/Au (27.5 kΩ·μm at 300 K),[53] and Au[54] (10 kΩ·μm at 300 K).

After a thorough examination of 12 sets of different 1D TiS_3 devices (Supporting Table 1), we established that In/Au contacts consistently exhibit lower contact resistance compared to Au and Cr/Au contacts. The contact resistance in our 1D In−TiS_3 devices advances toward the state-of-the-art values reported for 1D carbon nanotubes (90 Ω·μm).[55] Furthermore, we estimated a transfer length (Supporting Figure S8) of L_T = 100 ± 18 nm at 5 K and a carrier density of 8.6 × 10^{12} cm^{-2}, characterizing the contact length over which most of the charge transfer occurs. Notably, the transfer length is not limited by the contact length, which exceeds the L_T by a factor of 5, i.e., $L_T \ll L_C$, where the contact length $L_C \approx$ 500 nm.

To further highlight the differences between Cr/Au and In/Au contacts, we plotted the temperature dependence of the contacts' nonlinearity at low bias voltage defined as

https://doi.org/10.1021/acsnano.4c15086
ACS Nano 2025, 19, 10878−10888

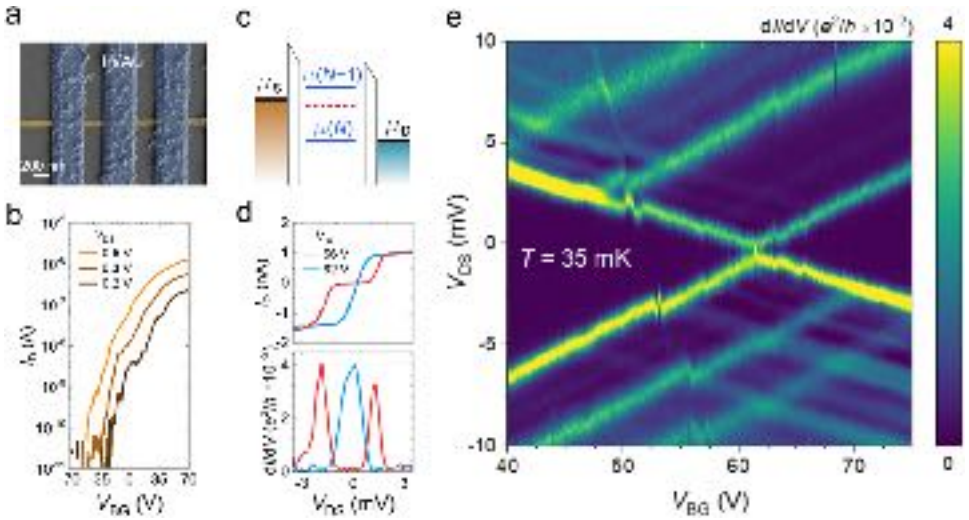

Figure 3. (a) False-color SEM image of the short-channel FET devices. The scale bar is 200 nm. (b) Typical transfer characteristics of a short-channel FET device at a temperature of 35 mK. (c) Schematic diagram of the chemical potential levels $\mu(N)$ and $\mu(N + 1)$ of a quantum dot, alongside the chemical potentials of the source and drain, μ_S and μ_D. The dashed line marks the level corresponding to a transition involving an excited state. (d) (Top) Output curves of the device revealing Coulomb staircase behavior at 35 mK, characteristic of the Coulomb blockade effect. (Bottom) Differential conductance corresponding to the Coulomb staircase in the top panel. (e) 2D color plot of the differential conductance as a function of drain−source bias V_{DS} and back-gate voltage V_{BG}, revealing the charge stability diagram of the quantum dot.

$$N = (d^2I_{DS}/dV_{DS}^2)/2(dI_{DS}/dV_{DS}) \quad (2)$$

A perfectly linear output curve corresponds to $N = 0$, whereas the higher nonlinearity values may indicate the presence of the non-negligible Schottky barriers. Figure 2g shows that output curves of In/Au contacts remain linear down to 5 K, whereas Cr/Au contacts exhibit linear characteristics only near room temperature and quickly become nonlinear at lower temperatures. Similarly, the nonlinearity of pure Au contacts consistently increases at temperatures below 300 K (Supporting Figure S7c). This observation is consistent with the temperature dependence of the contact resistance for In/Au and Cr/Au electrodes (Supporting Figure S5). While the contact resistance of Cr/Au−TiS_3 devices increases at low temperatures, the resistance of the In/Au contacts remains constant across the entire temperature range, confirming that carrier injection occurs via a field emission process rather than thermionic emission.

The low contact resistances provided by In/Au contacts enabled us to explore the low-temperature performance of TiS_3 NRs by measuring the charge-carrier mobility and gate-dependent conductivity down to 5 K. Figure 2h examines transfer characteristics of In−TiS_3 and Au−TiS_3 1D devices at a temperature of 5 K. While both devices exhibit transfer curves of a typical n-type FET, In/Au contacts enable enhanced conduction and a superior ON/OFF current ratio exceeding 10^4. We estimated the field-effect mobility in two-terminal devices and plotted the thermal evolution on a logarithmic scale in Figure 2i. Notably, the low contact resistance in In/Au devices ensures that the device performance is not limited by the contacts, as evidenced by similar characteristics observed in both two-terminal and four-terminal measurement configurations (Supporting Figure S9). At temperatures above 100 K, the electron mobility follows typical power-law behavior, $T^{-\gamma}$. At a carrier density of 3.5×10^{12} cm^{-2} (D1), we extracted an exponent $\gamma = 1.68$, which is higher than the $\gamma = 1.01$ obtained from the second device (D2) at a higher carrier density of 1.2×10^{13} cm^{-2} (see Supporting Table 1 for device parameters). Values of $\gamma \geqslant 1$ indicated that the dominant limiting mechanism is scattering by optical phonons, ascribed to deformation potential and Fröhlich interaction.[56] Notably, the range of γ values is consistent with those extracted from 1D graphene NRs[5] and flake-like 2D TiS_3 devices.[57] At lower temperatures, optical phonon scattering is suppressed, and the carrier mobility is primarily limited by scattering from acoustic phonons[58] and Coulomb interactions with impurities and atomic defects in TiS_3.[59,60] In our devices, the electron mobility at 5 K reaches approximately 52 cm^2 V^{-1} s^{-1} from device D1 and 97 cm^2 V^{-1} s^{-1} from device D2. These values mark an improvement over the previous reports on TiS_3 NRs (1.4−43 cm^2 V^{-1} s^{-1}).[18,26,27]

2.2. Coulomb Blockade in TiS_3 Quantum Dots. Motivated by the low resistance of In/Au contacts, we fabricated short-channel TiS_3 devices and performed charge transport measurements at 35 mK. An SEM image of the devices with a channel length of ∼200 nm is shown in Figure 3a (TiS_3 NR width and thickness are 97 ± 1 and 4.2 ± 0.2 nm, respectively). Our short-channel TiS_3 devices retain n-type semiconducting behavior with an ON/OFF ratio > 10^4 (Figure 3b, Supporting Figure S10) and an electron mobility of ∼30−40 cm^2 V^{-1} s^{-1} at a carrier density of 5×10^{12} cm^{-2}. At low drain−source bias (Figure 3d, top panel), the output curves reveal step-like behavior, characteristic of the Coulomb blockade effect.[61] In a quantum dot with N electrons in equilibrium, transport between two states occurs when the corresponding chemical potential, $\mu(N)$, lies within the bias window defined by source (μ_S) and drain (μ_D) chemical potentials, i.e., $\mu_S \geq \mu\ (N) \geq \mu_D$, for at least one value of N (Figure 3c). If this condition is not met, then current flow is restricted, resulting in a Coulomb blockade. A voltage applied to a capacitively-coupled gate shifts the chemical potentials for all N equally, which may lift the Coulomb blockade, allowing single-electron tunneling.[61]

https://doi.org/10.1021/acsnano.4c15086
ACS Nano 2025, 19, 10878−10888

To confirm this transport behavior, we measured differential conductance (dI/dV) as a function of the bias voltage V_{DS} and gate voltage V_{BG}. The bottom panel in Figure 3d shows differential conductance peaks associated with the steps in the output curves (top panel, Figure 3c). Figure 3e presents a 2D color map of the gate-dependent differential conductance at 35 mK, exhibiting a series of parallel lines on both the positive and negative sides of V_{DS}, resembling a typical charge stability diagram of a semiconductor quantum dot.[61] When the chemical potential of the dot is aligned with μ_S and μ_D at $V_{DS} = 0$, the electron tunneling occurs only at $V_{BG} \approx 62$ V, indicating a transition between two ground sates, GS(N) and GS($N + 1$). In the low-bias regime, the dot is in the Coulomb blockade for all of the other gate voltages.

Hereafter, we focus on the high-bias window that allows us to perform energy spectroscopy of the excited states.[62] Figure 4 illustrates a stability diagram schematic for the high-bias regime. The black dashed lines mark two transitions involving ground states, GS(N) and GS($N + 1$), which define the Coulomb blockade regime outside the V-shaped region. The set of white dashed lines denotes the transition involving excited states such as ES(N) and ES($N + 1$). Importantly, the energy level spacing can be extracted from this level diagram. For example, tracing the ES($N + 1$) line down until it terminates at the Coulomb blockade region yields an $\Delta E(N + 1) \approx 0.8$ meV. Figure 4 reveals several excited states all exhibiting a similar spacing of 0.8−0.9 meV. For a quantum dot, the level spacing is independent of the number of electrons and can be estimated using a particle-in-a-box model where $\Delta E = \pi\hbar^2/m^*A$. Here, $\hbar$ is the reduced Planck's constant ($h/2\pi$), m^* is an electron effective mass, and A is the area of the dot.[61] Using $m^* = 0.4m_e$,[44,63] we estimate the dot radius as $r \approx 8.7 \pm 0.1$ nm. In this device, the lithographically defined channel exceeds the size of the dot by an order of magnitude, suggesting that the dot likely originates from the charge inhomogeneity within the channel or is induced by a nonuniform screening effect from the substrate. Lastly, we note that the weak transitions in the tunneling region of the stability diagram may also be associated with the effects of gate bias on the contact leads.[64,65] However, these contributions cannot be unambiguously identified in the presented device architecture.

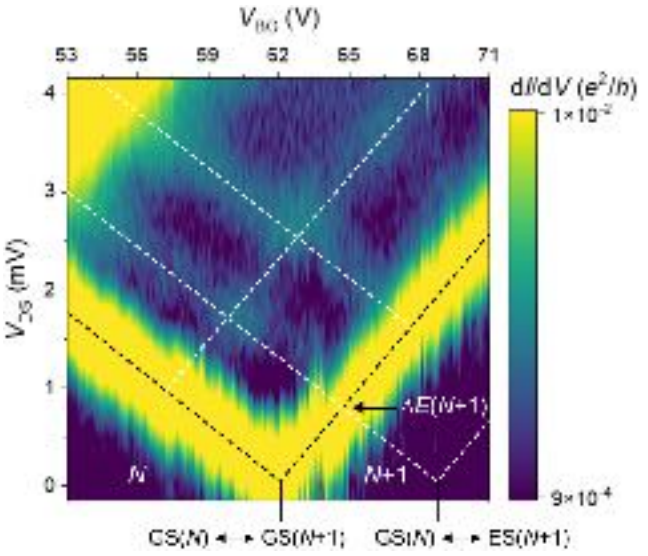

Figure 4. Charge stability diagram of the quantum dot in the positive drain−source bias window, revealing transitions involving ground states (black dashed lines) and excited states (white dashed lines). The differential conductance is plotted on a logarithmic color scale, highlighting weak transitions. The base temperature is 35 mK.

To gain insight into the spin character of the ground state of the quantum dot, we performed magnetospectroscopy measurements under a perpendicular magnetic field. As the magnetic field (B) lifts the spin degeneracy, the Pauli exclusion principle dictates the spin filling of the ground states. Figure 5a−c exhibits an evolution of the level diagram of the quantum dot under the external magnetic field. Here, adding a spin-up electron corresponds to a transition between GS(N) and GS($N + 1$) ground states (black dashed lines). However, the addition of a spin-down electron results in a transition from ground state GS(N) to excited state ES($N + 1$), separated by the Zeeman energy $\Delta E_Z = g\mu_B B$, where g is the electron g-factor and μ_B is the Bohr magneton. At a finite magnetic field, the transition to the excited state (Figure 5b,c, white dashed line) emerges inside the tunneling region. By analyzing the linear field dependence of the energy splitting between the ground and excited states, ΔE_Z, we extracted an electron g-factor $g = 1.8 \pm 3$. Typically, the out-of-plane g-factors in vdW QDs range between 0.8 and 15.8, depending on the material system and the nature of the quantum confinement.[66−68] Interestingly, our value is similar to the g-factor expected from a pure

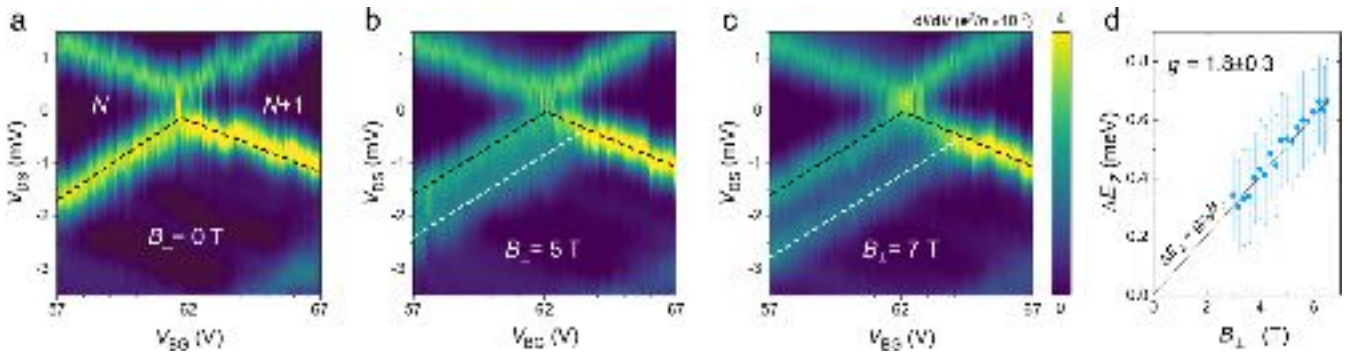

Figure 5. (a−c) 2D color maps of differential conductance at different magnetic fields: (a) $B = 0$ T, (b) 5 T, and (c) 7 T. The differential conductance at finite magnetic fields (b, c) reveals the emergence of an excited state (white dashed line) that shifts away from the ground state (black dashed line) by the Zeeman energy, ΔE_Z. (d) Zeeman energy at different magnetic fields (blue symbols) fitted with a linear function (solid black line).

https://doi.org/10.1021/acsnano.4c15086
ACS Nano 2025, 19, 10878−10888

spin-1/2 system, which may suggest a negligible role of other contributions to the magnetic field-dependent transport,[62] including the quantum dot size and electric field effects.[69,70] However, it should be noted that these effects may contribute to the total moment either additively or subtractively, depending on their nature and the direction of the magnetic field.[68] Further studies are needed to separate these effects and understand their effect on magnetic field-dependent transport in TiS_3 quantum dots.

3. CONCLUSIONS AND OUTLOOK ON NANOELECTRONICS AND QUANTUM APPLICATIONS

Natural 1D confinement and resilience to edge disorder in semiconducting layered NRs like TiS_3 offer a largely unexplored platform for down-scaled electronics. However, this potential can be hindered by high contact resistance, impeding further developments. In this work, we present a route to engineer vdW electrical contacts between a 3D metal and a 1D NR, enabling detailed evaluation of the charge transport in 1D TiS_3. Equipped with clean vdW contacts, thin and narrow NRs exhibit contact resistance as low as 2.7 ± 0.3 $k\Omega{\cdot}\mu m$, ensuring ohmic characteristics for TiS_3-based FETs at temperatures as low as 5 K. To the best of our knowledge, this is among the lowest contact resistance values reported for 1D vdW NRs. The extracted transfer length of $L_T = 100 \pm 18$ nm is comparable to advances in mature carbon nanotube transistor technology,[55] enabling contact down-scaling for a smaller device footprint in high-density circuits. Our theoretical calculations reveal a nondisruptive, dipole-like nature of the In−TiS_3 interface that facilitates efficient carrier injection. Throughout the 5−300 K temperature range, our FET devices demonstrate n-type conductivity, which can be actively modulated via electrostatic doping. At low temperatures, the field-effect carrier mobility reaches values up to ∼97 $cm^2\ V^{-1}\ s^{-1}$ at a carrier density of $1.2 \times 10^{13}\ cm^{-2}$. These values can be further improved by reducing the scattering from atomic defects in TiS_3 and minimizing Coulomb interactions at the channel interface. The latter can be achieved by encapsulating the NRs in a dielectric, such as hexagonal boron nitride (hBN), which has shown significant performance improvements in other vdW 1D FETs.[5] Particular emphasis must be placed on minimizing the density of the atomic defects. TiS_3 crystals are known to exhibit various defects, including sulfur vacancies that act as electron dopants and strongly alter the intrinsic carrier density.[53,71] Furthermore, tailoring morphology from 2D nanosheets to 1D NRs is accomplished by tuning the density of sulfur vacancies during synthesis through control of the growth temperature.[43] Higher defect densities are associated with the 2D morphology, which may suggest a reduced impact of in-plane anisotropy in the defective TiS_3. Further studies are needed to optimize the growth conditions for defect-free TiS_3 NRs.

Our work demonstrates the potential of TiS_3 NRs as a material platform for emerging technologies such as quantum sensing and information processing. Leveraging our high-quality contacts, we assessed quantum transport in two-probe short-channel FET devices at a temperature of 35 mK. The observed Coulomb blockade effect illustrates the proof-of-concept operation of a single-electron tunneling device within anisotropic 1D TiS_3. We performed excited state spectroscopy and magnetospectroscopy of the ground state, extracting an electron g-factor of $g = 1.8 \pm 0.3$. While this quantum dot likely originates from charge inhomogeneity within the channel or at the interface, further improvements in device fabrication and design modifications can lead to well-controlled quantum confinement shaped by crystal anisotropy and electrostatic fields, opening the route for high-accuracy sensing with single-electron transistors.[72−75] Notably, our stability diagrams over an extended gate range indicate the formation of a single quantum dot within an ∼200 nm channel. The clean stability diagrams suggest minimal contribution from edge disorder, which is often associated with uncontrollable states that significantly distort Coulomb blockade signatures.[76,77] The high quality of the stability diagrams allowed us to perform excited state spectroscopy, identifying single-electron tunneling events that are inaccessible in disordered devices. The intrinsic in-plane anisotropy 1D TiS_3 offers structural uniformity over tens of micrometers and resilience against edge disorder, benefiting the development of quantum dot devices for quantum metrology,[78−80] quantum tomography,[81,82] and providing a fertile ground for engineering spin-qubit arrays[83] toward the realization of analog quantum simulators.[84] Moreover, the vdW surface of TiS_3 NRs offers an ideal interface for engineering heterostructures with superconductors, free from strain and charge traps, paving the way for the realization of Kitaev chains and topological quantum computing.[85,86]

4. METHODS

4.1. Material Growth and Device Fabrication. TiS_3 crystals were grown via a self-flux process. Sulfur powder (0.96 g) and titanium wire (0.36 g) in a molar ratio of approximately 4:1 were loaded and vacuum-sealed (at 10^{-6} Torr) in a 2 mm thick quartz ampule. The sealed ampule was 23 cm long with a 16 mm outer diameter. The ampule was then heated to 750 °C at a ramp rate of 60 °C/h in a two-zone tube furnace, dwelt for 166 h, and cooled to 650−600 °C at a cooling rate of 0.6−0.9 °C/h; then, the furnace naturally cooled to room temperature. The long whiskers of TiS_3 were extracted from the ampule and stored under inert conditions of the Ar-filled glovebox.

Bulk TiS_3 whiskers were mechanically exfoliated with tape and transferred onto the Si/SiO_2 substrate. Conventional e-beam lithography (100 kV, 800 pA) with poly(methyl methacrylate) (PMMA) was used to define contacts and bonding pads. In/Au (5:50 nm) or Cr/Au (0.5:50 nm) metal contacts were deposited sequentially by thermal evaporation under a high vacuum (∼10^{-7} Torr). To minimize damage to the fragile surface of TiS_3, the sample crucible was cooled to 0 °C throughout the deposition process. Deposition rates of all metals were kept at 0.1 Å/s. After liftoff in MICROPOSIT 1165 remover, the devices were cleaned in acetone and ethanol and dried with Ar-gun. The entire device fabrication process was conducted inside the Ar-filled glovebox with O_2 and H_2O levels ≤ 0.1 ppm.

4.2. Electrical Measurements. Electrical measurements within the 300−5 K temperature range were carried out using a home-built cryogenic setup based on Janis ST500 cryostat equipped with a pulse-tube cryocooler. Two-terminal and four-terminal FET characteristics were obtained by using two Keithely 2450 source-measure units (SMUs).

Electrical measurements within the 0.035−2 K range were performed in the BLUEFORS XLD dilution refrigerator equipped with electron filters and a 9 T solenoid magnet. Device characteristics were obtained with a low-noise SPECS RC5 real-time controller, Nanonis Tramea DACs, and a Femto DLPCA-200 transimpedance amplifier.

4.3. Theoretical Calculations. DFT calculations were performed using the projected augmented wave method[87] and Generalized gradient approximation with Perdew−Burke−Ernzerhof functional[88] implemented in Vienna Ab initio Simulation Package.[89] For geometry

https://doi.org/10.1021/acsnano.4c15086
ACS Nano 2025, 19, 10878−10888

optimizations, $\frac{30}{a} \times \frac{30}{b} \times 1$, and for static calculations, $\frac{60}{a} \times \frac{60}{b} \times 1$ Monkhorst–Pack k-points grids were used, where a and b are the in-plane lattice parameters of a supercell. For all of the calculations, 520 eV kinetic energy cutoff and Gaussian smearing method with a smearing width of 0.05 eV have been used. Geometry optimizations were performed until the force on every atom fell below 0.02 eV Å^{-1}. The energy difference in successive iterations was set to 10^{-6} eV as the self-convergence criteria. For dispersion correction, Grimme DFT-D3[90] van der Waals interaction with zero-damping function was used. Dipole correction was applied along the out-of-plane direction to eliminate the pseudointeraction of the dipole moments.

QuantumATK interface builder module[91] was used to build metal–TiS_3 interfaces. For the interface design, six layers of (001)-cleaved surface of In and (111)-cleaved surface of Au were considered. To create an interface, the supercells of metal and TiS_3 surfaces were aligned first and then the strain was applied on the TiS_3 surface to match the aligned supercells. Sufficiently large supercells were designed to reduce the interface strain to below 1%. In–TiS_3 supercell consists of 108 atoms with lattice parameters of $a = b =$ 10.2 Å and mean strain on TiS_3 about 0.85%. Au–TiS_3 supercell contains 112 atoms with lattice parameters $a = 5.0$ and $b = 17.1$ Å and mean strain of about 0.65%. A vacuum layer of 20 Å was inserted along the z direction to eliminate any interaction between the two periodic replicas during DFT calculations. During relaxations, the bottom three layers of the metal atoms toward the vacuum side were fixed to emulate the nature of a bulk electrode.

ASSOCIATED CONTENT

Supporting Information

The Supporting Information is available free of charge at https://pubs.acs.org/doi/10.1021/acsnano.4c15086.

Material characterization; additional computational results; summary of device parameters and contact resistances; further data on temperature dependence; details on devices with Au contacts; transfer length method description; comparison of 2-probe and 4-probe measurements; and stability diagram of a clean device (PDF)

AUTHOR INFORMATION

Corresponding Authors

Ivan A. Verzhbitskiy − *Quantum Innovation Centre (Q. InC), Agency for Science Technology and Research (A*STAR), Singapore 138634, Republic of Singapore; Institute of Materials Research and Engineering (IMRE), Agency for Science Technology and Research (A*STAR), Singapore 138634, Republic of Singapore;* orcid.org/0000-0001-5945-8276; Email: ivan_verzhbitskiy@imre.a-star.edu.sg

Kuan Eng Johnson Goh − *Quantum Innovation Centre (Q. InC), Agency for Science Technology and Research (A*STAR), Singapore 138634, Republic of Singapore; Institute of Materials Research and Engineering (IMRE), Agency for Science Technology and Research (A*STAR), Singapore 138634, Republic of Singapore; Department of Physics, National University of Singapore, Singapore 117551, Singapore; Division of Physics and Applied Physics, School of Physical and Mathematical Sciences, Nanyang Technological University, Singapore 637371, Singapore;* orcid.org/0000-0003-0599-9696; Email: kejgoh@yahoo.com

Authors

Abhishek Mishra − *Quantum Innovation Centre (Q. InC), Agency for Science Technology and Research (A*STAR), Singapore 138634, Republic of Singapore; Institute of Materials Research and Engineering (IMRE), Agency for Science Technology and Research (A*STAR), Singapore 138634, Republic of Singapore;* orcid.org/0000-0002-1267-2440

Sanchali Mitra − *Science, Mathematics, and Technology, Singapore University of Technology and Design, Singapore 487372, Singapore*

Zhepeng Zhang − *Department of Physics, National University of Singapore, Singapore 117551, Singapore*

Sarthak Das − *Quantum Innovation Centre (Q. InC), Agency for Science Technology and Research (A*STAR), Singapore 138634, Republic of Singapore; Institute of Materials Research and Engineering (IMRE), Agency for Science Technology and Research (A*STAR), Singapore 138634, Republic of Singapore;* orcid.org/0000-0001-9526-9819

Chit Siong Lau − *Quantum Innovation Centre (Q. InC), Agency for Science Technology and Research (A*STAR), Singapore 138634, Republic of Singapore; Institute of Materials Research and Engineering (IMRE), Agency for Science Technology and Research (A*STAR), Singapore 138634, Republic of Singapore; Science, Mathematics, and Technology, Singapore University of Technology and Design, Singapore 487372, Singapore;* orcid.org/0000-0002-6590-070X

Rainer Lee − *Quantum Innovation Centre (Q. InC), Agency for Science Technology and Research (A*STAR), Singapore 138634, Republic of Singapore; Institute of Materials Research and Engineering (IMRE), Agency for Science Technology and Research (A*STAR), Singapore 138634, Republic of Singapore*

Ding Huang − *Quantum Innovation Centre (Q. InC), Agency for Science Technology and Research (A*STAR), Singapore 138634, Republic of Singapore; Institute of Materials Research and Engineering (IMRE), Agency for Science Technology and Research (A*STAR), Singapore 138634, Republic of Singapore*

Goki Eda − *Department of Physics, National University of Singapore, Singapore 117551, Singapore; Centre for Advanced 2D Materials, National University of Singapore, Singapore 117546, Singapore; Department of Chemistry, National University of Singapore, Singapore 117543, Singapore;* orcid.org/0000-0002-1575-8020

Yee Sin Ang − *Science, Mathematics, and Technology, Singapore University of Technology and Design, Singapore 487372, Singapore;* orcid.org/0000-0002-1637-1610

Complete contact information is available at: https://pubs.acs.org/10.1021/acsnano.4c15086

Notes

The authors declare no competing financial interest.

ACKNOWLEDGMENTS

The authors acknowledge Dr. FengXia Wei and Dr. Chew Li Tian for their help with XRD measurements and analysis. This research was supported by the Agency for Science, Technology, and Research (A*STAR) (#21709, C230917006, C230917007). I.A.V. and K.E.J.G. acknowledge support from a Singapore National Research Foundation Grant (CRP21-2018-0001). Y.S.A. and S.M. are supported by the Singapore Ministry of Education (MOE) Academic Research Fund (AcRF) Tier 2 Grant (MOE-T2EP50221-0019). Y. S. A. is also supported by the SMU-SUTD Joint Grant (Award No. 22-SIS-SMU-054). The computational work for this work was

partially performed on resources of the National Supercomputing Centre, Singapore (https://www.nscc.sg). C.S.L. acknowledges support from A*STAR MTC YIRG grant no. M21K3c0124 and MTC IRG grant no. M23M6c0103. D.H. acknowledges funding support from A*STAR Project C222812022 and MTC YIRG M22K3c0105. G.E. acknowledges support from the Ministry of Education (MOE), Singapore, under AcRF Tier 3 (MOE2018-T3-1-005) and Tier 1 (A-8001995-00-00).

REFERENCES

(1) Lemme, M. C.; Akinwande, D.; Huyghebaert, C.; Stampfer, C. 2D materials for future heterogeneous electronics. *Nat. Commun.* **2022**, *13*, No. 1392.
(2) Wang, H.; Wang, H. S.; Ma, C.; Chen, L.; Jiang, C.; Chen, C.; Xie, X.; Li, A.-P.; Wang, X. Graphene nanoribbons for quantum electronics. *Nat. Rev. Phys.* **2021**, *3*, 791−802.
(3) Meng, Y.; Wang, W.; Ho, J. C. One-Dimensional Atomic Chains for Ultimate-Scaled Electronics. *ACS Nano* **2022**, *16*, 13314−13322.
(4) Balandin, A. A.; Kargar, F.; Salguero, T. T.; Lake, R. K. One-dimensional van der Waals quantum materials. *Mater. Today* **2022**, *55*, 74−91.
(5) Lyu, B.; Chen, J.; Wang, S.; Lou, S.; Shen, P.; Xie, J.; Qiu, L.; Mitchell, I.; Li, C.; Hu, C.; et al. Graphene nanoribbons grown in hBN stacks for high-performance electronics. *Nature* **2024**, *628*, 758−764.
(6) Correa, J. H.; Dias, A. C.; Villegas-Lelovsky, L.; Fu, J.; Chico, L.; Qu, F. Anisotropy of the spin-polarized edge current in monolayer transition metal dichalcogenide zigzag nanoribbons. *Phys. Rev. B* **2020**, *101*, 195422.
(7) Gut, D.; Prokop, M.; Sticlet, D.; Nowak, M. P. Valley polarized current and resonant electronic transport in a nonuniform MoS_2 zigzag nanoribbon. *Phys. Rev. B* **2020**, *101*, 085425.
(8) Nakada, K.; Fujita, M.; Dresselhaus, G.; Dresselhaus, M. S. Edge state in graphene ribbons: Nanometer size effect and edge shape dependence. *Phys. Rev. B* **1996**, *54*, 17954−17961.
(9) Son, Y.-W.; Cohen, M. L.; Louie, S. G. Energy Gaps in Graphene Nanoribbons. *Phys. Rev. Lett.* **2006**, *97*, 216803.
(10) Chowdhury, T.; Sadler, E. C.; Kempa, T. J. Progress and Prospects in Transition-Metal Dichalcogenide Research Beyond 2D. *Chem. Rev.* **2020**, *120*, 12563−12591.
(11) Chen, Z.; Narita, A.; Müllen, K. Graphene nanoribbons: on-surface synthesis and integration into electronic devices. *Adv. Mater.* **2020**, *32*, 2001893.
(12) Bischoff, D.; et al. Localized charge carriers in graphene nanodevices. *Appl. Phys. Rev.* **2015**, *2* (3), 031301.
(13) Kotekar-Patil, D.; Deng, J.; Wong, S. L.; Goh, K. E. J. Coulomb Blockade in Etched Single- and Few-Layer MoS2 Nanoribbons. *ACS Appl. Electron. Mater.* **2019**, *1*, 2202−2207.
(14) Island, J. O.; Molina-Mendoza, A. J.; Barawi, M.; Biele, R.; Flores, E.; Clamagirand, J. M.; Ares, J. R.; Sánchez, C.; Van Der Zant, H. S.; D'Agosta, R.; et al. Electronics and optoelectronics of quasi-1D layered transition metal trichalcogenides. *2D Mater.* **2017**, *4*, 022003.
(15) Island, J. O.; Biele, R.; Barawi, M.; Clamagirand, J. M.; Ares, J. R.; Sánchez, C.; Van Der Zant, H. S.; Ferrer, I. J.; D'Agosta, R.; Castellanos-Gomez, A. Titanium trisulfide (TiS3): a 2D semiconductor with quasi-1D optical and electronic properties. *Sci. Rep.* **2016**, *6*, No. 22214.
(16) Liu, H.; Yu, X.; Wu, K.; Gao, Y.; Tongay, S.; Javey, A.; Chen, L.; Hong, J.; Wu, J. Extreme in-plane thermal conductivity anisotropy in titanium trisulfide caused by heat-carrying optical phonons. *Nano Lett.* **2020**, *20*, 5221−5227.
(17) Liu, C.; Wu, C.; Tan, X. Y.; Tao, Y.; Zhang, Y.; Li, D.; Yang, J.; Yan, Q.; Chen, Y. Unexpected doping effects on phonon transport in quasi-one-dimensional van der Waals crystal TiS3 nanoribbons. *Nat. Commun.* **2023**, *14*, No. 5597.
(18) Island, J. O.; Buscema, M.; Barawi, M.; Clamagirand, J. M.; Ares, J. R.; Sánchez, C.; Ferrer, I. J.; Steele, G. A.; van der Zant, H. S.; Castellanos-Gomez, A. Ultrahigh photoresponse of few-layer TiS3 nanoribbon transistors *arXiv preprint arXiv:1406.5003* 2014; Vol. *2* DOI: 10.1002/adom.201400043.
(19) Niu, Y.; Frisenda, R.; Flores, E.; Ares, J. R.; Jiao, W.; Perez de Lara, D.; Sanchez, C.; Wang, R.; Ferrer, I. J.; Castellanos-Gomez, A. Polarization-Sensitive and Broadband Photodetection Based on a Mixed-Dimensionality TiS3/Si p−n Junction. *Adv. Opt. Mater.* **2018**, *6*, 1800351.
(20) Lipatov, A.; Loes, M. J.; Lu, H.; et al. Quasi-1D TiS3 Nanoribbons: Mechanical Exfoliation and Thickness-Dependent Raman Spectroscopy. *ACS Nano* **2018**, *12*, 12713−12720.
(21) Kang, J.; Sahin, H.; Ozaydin, H. D.; Senger, R. T.; Peeters, F. TiS_3 nanoribbons: Width-independent band gap and strain-tunable electronic properties. *Phys. Rev. B* **2015**, *92*, 075413.
(22) Kang, J.; Wang, L.-W. Robust band gap of TiS3 nanofilms. *Phys. Chem. Chem. Phys.* **2016**, *18*, 14805−14809.
(23) Lu, W.; Ji, Z.; Pfeiffer, L.; West, K.; Rimberg, A. Real-time detection of electron tunnelling in a quantum dot. *Nature* **2003**, *423*, 422−425.
(24) Blumenthal, M. D.; Kaestner, B.; Li, L.; Giblin, S.; Janssen, T.; Pepper, M.; Anderson, D.; Jones, G.; Ritchie, D. Gigahertz quantized charge pumping. *Nat. Phys.* **2007**, *3*, 343−347.
(25) Gorlova, I.; Zybtsev, S.; Pokrovskii, V. Y.; Bolotina, N.; Gavrilkin, S. Y.; Tsvetkov, A. Y. Magnetotransport and power-law I−V curves of the layered quasi one-dimensional compound TiS3. *Phys. B* **2015**, *460*, 11−15.
(26) Lipatov, A.; Wilson, P. M.; Shekhirev, M.; Teeter, J. D.; Netusil, R.; Sinitskii, A. Few-layered titanium trisulfide (TiS 3) field-effect transistors. *Nanoscale* **2015**, *7*, 12291−12296.
(27) Randle, M.; Lipatov, A.; Kumar, A.; et al. Gate-Controlled Metal−Insulator Transition in TiS3 Nanowire Field-Effect Transistors. *ACS Nano* **2019**, *13*, 803−811.
(28) Gorlova, I. G.; Pokrovskii, V. Y.; Frolov, A. V.; Orlov, A. P. Comment on "Gate-Controlled Metal−Insulator Transition in TiS3 Nanowire Field-Effect Transistors. *ACS Nano* **2019**, *13*, 8495−8497.
(29) Randle, M. D.; Lipatov, A.; Datta, A.; Kumar, A.; Mansaray, I.; Sinitskii, A.; Singisetti, U.; Han, J. E.; Bird, J. P. High-electric-field behavior of the metal-insulator transition in TiS3 nanowire transistors. *Appl. Phys. Lett.* **2022**, *120*, 073102.
(30) Allain, A.; Kang, J.; Banerjee, K.; Kis, A. Electrical contacts to two-dimensional semiconductors. *Nat. Mater.* **2015**, *14*, 1195−1205.
(31) Lau, C. S.; Chee, J. Y.; Ang, Y. S.; Tong, S. W.; Cao, L.; Ooi, Z.-E.; Wang, T.; Ang, L. K.; Wang, Y.; Chhowalla, M.; Goh, K. E. J. Quantum Transport in Two-Dimensional WS2 with High-Efficiency Carrier Injection through Indium Alloy Contacts. *ACS Nano* **2020**, *14*, 13700−13708. PMID: 32915542.
(32) Grabert, H.; Devoret, M. *Single Charge Tunneling: Coulomb Blockade Phenomena In Nanostructures*, NATO Science Series B; Springer: New York, NY, 1992.
(33) Likharev, K. Single-electron devices and their applications. *Proc. IEEE* **1999**, *87*, 606−632.
(34) Lau, C. S.; Chee, J. Y.; Cao, L.; et al. Gate-Defined Quantum Confinement in CVD 2D WS2. *Adv. Mater.* **2022**, *34*, 2103907.
(35) Franklin, A. D.; Hersam, M. C.; Wong, H.-S. P. Carbon nanotube transistors: Making electronics from molecules. *Science* **2022**, *378*, 726−732.
(36) Morkoç, H.; Strite, S.; Gao, G. B.; Lin, M. E.; Sverdlov, B.; Burns, M. Large-band-gap SiC, III-V nitride, and II-VI ZnSe-based semiconductor device technologies. *J. Appl. Phys.* **1994**, *76*, 1363−1398.
(37) Ang, Y. S.; Cao, L.; Ang, L. K. Physics of electron emission and injection in two-dimensional materials: Theory and simulation. *InfoMat* **2021**, *3*, 502−535.
(38) Wang, Y.; Chhowalla, M. Making clean electrical contacts on 2D transition metal dichalcogenides. *Nat. Rev. Phys.* **2022**, *4*, 101−112.
(39) Wu, R. J.; Udyavara, S.; Ma, R.; Wang, Y.; Chhowalla, M.; Birol, T.; Koester, S. J.; Neurock, M.; Mkhoyan, K. A. Visualizing the metal-

MoS_2 contacts in two-dimensional field-effect transistors with atomic resolution. *Phys. Rev. Mater.* **2019**, *3*, 111001.
(40) Kim, C.; Moon, I.; Lee, D.; Choi, M. S.; Ahmed, F.; Nam, S.; Cho, Y.; Shin, H.-J.; Park, S.; Yoo, W. J. Fermi Level Pinning at Electrical Metal Contacts of Monolayer Molybdenum Dichalcogenides. *ACS Nano* **2017**, *11*, 1588−1596.
(41) Poljak, M.; Matić, M.; Zeljko, A. Impact of Contact Configuration on Contact Resistance in Ultranarrow Graphene Nanoribbon Devices. *IEEE Trans. Electron Devices* **2022**, *69*, 5283−5288.
(42) Wang, Y.; Kim, J. C.; Wu, R. J.; Martinez, J.; Song, X.; Yang, J.; Zhao, F.; Mkhoyan, A.; Jeong, H. Y.; Chhowalla, M. Van der Waals contacts between three-dimensional metals and two-dimensional semiconductors. *Nature* **2019**, *568*, 70−74.
(43) Island, J. O.; Barawi, M.; Biele, R.; Almazán, A.; Clamagirand, J. M.; Ares, J. R.; Sánchez, C.; van der Zant, H. S. J.; Álvarez, J. V.; D'Agosta, R.; Ferrer, I. J.; Castellanos-Gomez, A. TiS3 Transistors with Tailored Morphology and Electrical Properties. *Adv. Mater.* **2015**, *27*, 2595−2601.
(44) Dai, J.; Zeng, X. C. Titanium Trisulfide Monolayer: Theoretical Prediction of a New Direct-Gap Semiconductor with High and Anisotropic Carrier Mobility. *Angew. Chem., Int. Ed.* **2015**, *54*, 7572−7576.
(45) Liu, Y.; Guo, J.; Zhu, E.; Liao, L.; Lee, S.-J.; Ding, M.; Shakir, I.; Gambin, V.; Huang, Y.; Duan, X. Approaching the Schottky-Mott limit in van der Waals metal-semiconductor junctions. *Nature* **2018**, *557*, 696−700.
(46) Liu, X.; Choi, M. S.; Hwang, E.; Yoo, W. J.; Sun, J. Fermi Level Pinning Dependent 2D Semiconductor Devices: Challenges and Prospects. *Adv. Mater.* **2022**, *34*, 2108425.
(47) Chanana, A.; Mahapatra, S. Prospects of zero Schottky barrier height in a graphene-inserted MoS2-metal interface. *J. Appl. Phys.* **2016**, *119*, 014303.
(48) Cui, X.; Shih, E.-M.; Jauregui, L. A.; Chae, S. H.; Kim, Y. D.; Li, B.; Seo, D.; Pistunova, K.; Yin, J.; Park, J.-H.; et al. Low-temperature ohmic contact to monolayer MoS2 by van der Waals bonded Co/h-BN electrodes. *Nano Lett.* **2017**, *17*, 4781−4786.
(49) Chen, R.-S.; Ding, G.; Zhou, Y.; Han, S.-T. Fermi-level depinning of 2D transition metal dichalcogenide transistors. *J. Mater. Chem. C* **2021**, *9*, 11407−11427.
(50) Wang, Q.; Shao, Y.; Shi, X. Mechanism of charge redistribution at the metal-semiconductor and semiconductor-semiconductor interfaces of metal-bilayer MoS2 junctions. *J. Chem. Phys.* **2020**, *152*, 244701.
(51) Liu, W.; Chikkadi, K.; Muoth, M.; Hierold, C.; Haluska, M. The impact of Cr adhesion layer on CNFET electrical characteristics. *Nanotechnology* **2016**, *27*, 015201.
(52) Fathipour, S.; Remskar, M.; Varlec, A.; Ajoy, A.; Yan, R.; Vishwanath, S.; Rouvimov, S.; Hwang, W. S.; Xing, H. G.; Jena, D.; Seabaugh, A. Synthesized multiwall MoS2 nanotube and nanoribbon field-effect transistors. *Appl. Phys. Lett.* **2015**, *106*, 022114.
(53) Sun, M.; Li, J.; Ji, Q.; Lin, Y.; Wang, J.; Su, C.; Chiu, M.-H.; Sun, Y.; Si, H.; Palacios, T.; Lu, J.; Xie, D.; Kong, J. Anomalous heavy doping in chemical-vapor-deposited titanium trisulfide nanostructures. *Phys. Rev. Mater.* **2021**, *5*, 094002.
(54) Gilbert, S. J.; Lipatov, A.; Yost, A. J.; Loes, M. J.; Sinitskii, A.; Dowben, P. A. The electronic properties of Au and Pt metal contacts on quasi-one-dimensional layered TiS3(001). *Appl. Phys. Lett.* **2019**, *114*, 101604.
(55) Lin, Y.; Cao, Y.; Ding, S.; Zhang, P.; Xu, L.; Liu, C.; Hu, Q.; Jin, C.; Peng, L.-M.; Zhang, Z. Scaling aligned carbon nanotube transistors to a sub-10 nm node. *Nat. Electron.* **2023**, *6*, 506−515.
(56) Kaasbjerg, K.; Thygesen, K. S.; Jacobsen, K. W. Phonon-limited mobility in n-type single-layer MoS_2 from first principles. *Phys. Rev. B* **2012**, *85*, 115317.
(57) Papadopoulos, N.; Flores, E.; Watanabe, K.; Taniguchi, T.; Ares, J. R.; Sanchez, C.; Ferrer, I. J.; Castellanos-Gomez, A.; Steele, G. A.; Van Der Zant, H. S. Multi-terminal electronic transport in boron nitride encapsulated TiS3 nanosheets. *2D Mater.* **2020**, *7*, 015009.
(58) Kaasbjerg, K.; Thygesen, K. S.; Jauho, A.-P. Acoustic phonon limited mobility in two-dimensional semiconductors: Deformation potential and piezoelectric scattering in monolayer MoS_2 from first principles. *Phys. Rev. B* **2013**, *87*, 235312.
(59) Ando, T.; Fowler, A. B.; Stern, F. Electronic properties of two-dimensional systems. *Rev. Mod. Phys.* **1982**, *54*, 437−672.
(60) Das Sarma, S.; Adam, S.; Hwang, E. H.; Rossi, E. Electronic transport in two-dimensional graphene. *Rev. Mod. Phys.* **2011**, *83*, 407−470.
(61) Kouwenhoven, L. P.; Marcus, C. M.; McEuen, P. L.; Tarucha, S.; Westervelt, R. M.; Wingreen, N. S. Chapter Electron Transport in Quantum Dots. In *Mesoscopic Electron Transport*; Sohn, L. L.; Kouwenhoven, L. P.; Schön, G., Eds.; Springer Science + Business Media: Dordrecht, 2013; pp 105−214.
(62) Hanson, R.; Kouwenhoven, L. P.; Petta, J. R.; Tarucha, S.; Vandersypen, L. M. K. Spins in few-electron quantum dots. *Rev. Mod. Phys.* **2007**, *79*, 1217−1265.
(63) Zhang, J.; Liu, X.; Wen, Y.; Shi, L.; Chen, R.; Liu, H.; Shan, B. Titanium Trisulfide Monolayer as a Potential Thermoelectric Material: A First-Principles-Based Boltzmann Transport Study. *ACS Appl. Mater. Interfaces* **2017**, *9*, 2509−2515.
(64) Möttönen, M.; Tan, K. Y.; Chan, K. W.; Zwanenburg, F. A.; Lim, W. H.; Escott, C. C.; Pirkkalainen, J.-M.; Morello, A.; Yang, C.; van Donkelaar, J. A.; Alves, A. D. C.; Jamieson, D. N.; Hollenberg, L. C. L.; Dzurak, A. S. Probe and control of the reservoir density of states in single-electron devices. *Phys. Rev. B* **2010**, *81*, 161304.
(65) Escott, C. C.; Zwanenburg, F. A.; Morello, A. Resonant tunnelling features in quantum dots. *Nanotechnology* **2010**, *21*, 274018.
(66) Davari, S.; Stacy, J.; Mercado, A.; Tull, J.; Basnet, R.; Pandey, K.; Watanabe, K.; Taniguchi, T.; Hu, J.; Churchill, H. Gate-Defined Accumulation-Mode Quantum Dots in Monolayer and Bilayer WSe_2. *Phys. Rev. Appl.* **2020**, *13*, 054058.
(67) Papadopoulos, N.; Gehring, P.; Watanabe, K.; Taniguchi, T.; van der Zant, H. S. J.; Steele, G. A. Tunneling spectroscopy of localized states of WS_2 barriers in vertical van der Waals heterostructures. *Phys. Rev. B* **2020**, *101*, 165303.
(68) Krishnan, R.; Biswas, S.; Hsueh, Y.-L.; Ma, H.; Rahman, R.; Weber, B. Spin-Valley Locking for In-Gap Quantum Dots in a MoS2 Transistor. *Nano Lett.* **2023**, *23*, 6171−6177.
(69) Björk, M. T.; Fuhrer, A.; Hansen, A. E.; Larsson, M. W.; Fröberg, L. E.; Samuelson, L. Tunable effective g factor in InAs nanowire quantum dots. *Phys. Rev. B* **2005**, *72*, 201307.
(70) Csonka, S.; Hofstetter, L.; Freitag, F.; Oberholzer, S.; Schönenberger, C.; Jespersen, T. S.; Aagesen, M.; Nygård, J. Giant Fluctuations and Gate Control of the g-Factor in InAs Nanowire Quantum Dots. *Nano Lett.* **2008**, *8*, 3932−3935.
(71) Iyikanat, F.; Sahin, H.; Senger, R. T.; Peeters, F. M. Vacancy Formation and Oxidation Characteristics of Single Layer TiS3. *J. Phys. Chem. C* **2015**, *119*, 10709−10715.
(72) Devoret, M. H.; Schoelkopf, R. J. Amplifying quantum signals with the single-electron transistor. *Nature* **2000**, *406*, 1039−1046.
(73) Blakesley, J. C.; See, P.; Shields, A. J.; Kardynał, B. E.; Atkinson, P.; Farrer, I.; Ritchie, D. A. Efficient Single Photon Detection by Quantum Dot Resonant Tunneling Diodes. *Phys. Rev. Lett.* **2005**, *94*, 067401.
(74) Morello, A.; Pla, J. J.; Zwanenburg, F. A.; Chan, K. W.; Tan, K. Y.; Huebl, H.; Möttönen, M.; Nugroho, C. D.; Yang, C.; Van Donkelaar, J. A.; et al. Single-shot readout of an electron spin in silicon. *Nature* **2010**, *467*, 687−691.
(75) Asgari, M.; Coquillat, D.; Menichetti, G.; Zannier, V.; Diakonova, N.; Knap, W.; Sorba, L.; Viti, L.; Vitiello, M. S. Quantum-Dot Single-Electron Transistors as Thermoelectric Quantum Detectors at Terahertz Frequencies. *Nano Lett.* **2021**, *21*, 8587−8594.
(76) Gallagher, P.; Todd, K.; Goldhaber-Gordon, D. Disorder-induced gap behavior in graphene nanoribbons. *Phys. Rev. B* **2010**, *81*, 115409.

https://doi.org/10.1021/acsnano.4c15086
ACS Nano 2025, 19, 10878−10888

(77) Han, M. Y.; Brant, J. C.; Kim, P. Electron Transport in Disordered Graphene Nanoribbons. *Phys. Rev. Lett.* **2010**, *104*, 056801.
(78) Pekola, J. P.; Saira, O.-P.; Maisi, V. F.; Kemppinen, A.; Möttönen, M.; Pashkin, Y. A.; Averin, D. V. Single-electron current sources: Toward a refined definition of the ampere. *Rev. Mod. Phys.* **2013**, *85*, 1421−1472.
(79) Giblin, S. P.; Fujiwara, A.; Yamahata, G.; Bae, M.-H.; Kim, N.; Rossi, A.; Möttönen, M.; Kataoka, M. Evidence for universality of tunable-barrier electron pumps. *Metrologia* **2019**, *56*, 044004.
(80) Scherer, H.; Schumacher, H. W. Single-Electron Pumps and Quantum Current Metrology in the Revised SI. *Ann. Phys.* **2019**, *531*, 1800371.
(81) Bisognin, R.; Marguerite, A.; Roussel, B.; Kumar, M.; Cabart, C.; Chapdelaine, C.; Mohammad-Djafari, A.; Berroir, J.-M.; Bocquillon, E.; Plaçais, B. Quantum tomography of electrical currents. *Nat. Commun.* **2019**, *10*, No. 3379.
(82) Fletcher, J. D.; Johnson, N.; Locane, E.; See, P.; Griffiths, J.; Farrer, I.; Ritchie, D.; Brouwer, P.; Kashcheyevs, V.; Kataoka, M. Continuous-variable tomography of solitary electrons. *Nat. Commun.* **2019**, *10*, No. 5298.
(83) Zajac, D. M.; Hazard, T. M.; Mi, X.; Nielsen, E.; Petta, J. R. Scalable Gate Architecture for a One-Dimensional Array of Semiconductor Spin Qubits. *Phys. Rev. Appl.* **2016**, *6*, 054013.
(84) Kiczynski, M.; Gorman, S.; Geng, H.; Donnelly, M.; Chung, Y.; He, Y.; Keizer, J.; Simmons, M. Engineering topological states in atom-based semiconductor quantum dots. *Nature* **2022**, *606*, 694−699.
(85) Dvir, T.; Wang, G.; van Loo, N.; Liu, C.-X.; Mazur, G. P.; Bordin, A.; Ten Haaf, S. L.; Wang, J.-Y.; van Driel, D.; Zatelli, F.; et al. Realization of a minimal Kitaev chain in coupled quantum dots. *Nature* **2023**, *614*, 445−450.
(86) Bordin, A.; Liu, C.-X.; Dvir, T.; Zatelli, F.; ten Haaf, S. L.; van Driel, D.; Wang, G.; van Loo, N.; van Caekenberghe, T.; Wolff, J. C.et al. Signatures of Majorana protection in a three-site Kitaev chain *arXiv preprint arXiv:2402.19382* 2024.
(87) Blöchl, P. E. Projector augmented-wave method. *Phys. Rev. B* **1994**, *50*, 17953−17979.
(88) Perdew, J. P.; Burke, K.; Ernzerhof, M. Generalized Gradient Approximation Made Simple. *Phys. Rev. Lett.* **1996**, *77*, 3865−3868.
(89) Kresse, G.; Joubert, D. From ultrasoft pseudopotentials to the projector augmented-wave method. *Phys. Rev. B* **1999**, *59*, 1758−1775.
(90) Moellmann, J.; Grimme, S. DFT-D3 Study of Some Molecular Crystals. *J. Phys. Chem. C* **2014**, *118*, 7615−7621.
(91) Stradi, D.; Jelver, L.; Smidstrup, S.; Stokbro, K. Method for determining optimal supercell representation of interfaces. *J. Phys.: Condens. Matter* **2017**, *29*, 185901.

https://doi.org/10.1021/acsnano.4c15086
ACS Nano 2025, 19, 10878−10888